



Hapke modeling of Rhea surface properties through Cassini-VIMS spectra

M. Ciarniello, F. Capaccioni, G. Filacchione, R.N. Clark, D.P. Cruikshank, P. Cerroni, A. Coradini, R.H. Brown, B.J. Buratti, F. Tosi, et al.

► To cite this version:

M. Ciarniello, F. Capaccioni, G. Filacchione, R.N. Clark, D.P. Cruikshank, et al.. Hapke modeling of Rhea surface properties through Cassini-VIMS spectra. *Icarus*, 2011, 214 (2), pp.541. <10.1016/j.icarus.2011.05.010>. <hal-00786875>

HAL Id: hal-00786875

<https://hal.science/hal-00786875v1>

Submitted on 11 Feb 2013

HAL is a multi-disciplinary open access archive for the deposit and dissemination of scientific research documents, whether they are published or not. The documents may come from teaching and research institutions in France or abroad, or from public or private research centers.

L'archive ouverte pluridisciplinaire **HAL**, est destinée au dépôt et à la diffusion de documents scientifiques de niveau recherche, publiés ou non, émanant des établissements d'enseignement et de recherche français ou étrangers, des laboratoires publics ou privés.



HAL Authorization

Accepted Manuscript

Hapke modeling of Rhea surface properties through Cassini-VIMS spectra

M. Ciarniello, F. Capaccioni, G. Filacchione, R.N. Clark, D.P. Cruikshank, P. Cerroni, A. Coradini, R.H. Brown, B.J. Buratti, F. Tosi, K. Stephan

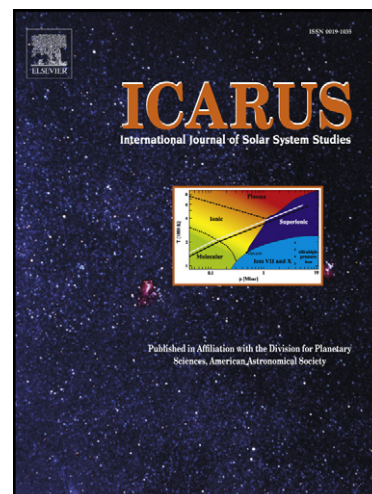
PII: S0019-1035(11)00175-8
DOI: [10.1016/j.icarus.2011.05.010](https://doi.org/10.1016/j.icarus.2011.05.010)
Reference: YICAR 9817

To appear in: *Icarus*

Received Date: 18 January 2011
Revised Date: 9 May 2011
Accepted Date: 10 May 2011

Please cite this article as: Ciarniello, M., Capaccioni, F., Filacchione, G., Clark, R.N., Cruikshank, D.P., Cerroni, P., Coradini, A., Brown, R.H., Buratti, B.J., Tosi, F., Stephan, K., Hapke modeling of Rhea surface properties through Cassini-VIMS spectra, *Icarus* (2011), doi: [10.1016/j.icarus.2011.05.010](https://doi.org/10.1016/j.icarus.2011.05.010)

This is a PDF file of an unedited manuscript that has been accepted for publication. As a service to our customers we are providing this early version of the manuscript. The manuscript will undergo copyediting, typesetting, and review of the resulting proof before it is published in its final form. Please note that during the production process errors may be discovered which could affect the content, and all legal disclaimers that apply to the journal pertain.



Hapke modeling of Rhea surface properties through Cassini-VIMS spectra

M. Ciarniello^{1*}, F. Capaccioni¹, G. Filacchione¹, R. N. Clark², D. P. Cruikshank³, P. Cerroni¹, A. Coradini⁴, R. H. Brown⁵, B. J. Buratti⁶, F. Tosi⁴, K. Stephan⁷

¹INAF-IASF, via del Fosso del Cavaliere, 100, Rome, Italy

²U.S. Geological Survey, Federal Center, Denver, CO 80225 USA

³NASA Ames Research Center, Moffett Field, CA 94035 USA

⁴INAF-IFSI, via del Fosso del Cavaliere, 100, Rome, Italy

⁵Lunar and Planetary Lab and Steward Observatory, University of Arizona, Tucson, AZ 85721
USA

⁶Jet Propulsion Laboratory, California Institute of Technology, Pasadena, CA 91109 USA

⁷Institute for Planetary Exploration, DLR, Berlin, Germany

Manuscript Pages: 43

Number of Tables: 4

Number of Figures: 12

Proposed Running Head: Hapke modeling of Rhea surface properties through Cassini-VIMS spectra

***Corresponding author:** Mauro Ciarniello

INAF-IASF Istituto di Astrofisica Spaziale e Fisica Cosmica

Via del Fosso del Cavaliere, 100, 00133 Rome, Italy

Phone: (0039)(06) 45488689

Email: mauro.ciarniello@iasf-roma.inaf.it

Abstract

The surface properties of the icy bodies in the saturnian system have been investigated by means of the CASSINI- VIMS (Visual Infrared Mapping Spectrometer) hyperspectral imager which operates in the 0.35-5.1 μm wavelength range. In particular, we have analyzed 111 full disk hyperspectral images of Rhea ranging in solar phase between 0.08° and 109.8° . These data have been previously analyzed by Filacchione et al. (2007, 2010) to study, adopting various “spectral indicators” (such as spectral slopes, band depth, continuum level, etc.), the relations among various saturnian satellites. As a further step we proceed in this paper to a quantitative evaluation of the physical parameters determining the spectrophotometric properties of Rhea’s surface. To do this we have applied Hapke

(1993) IMSA model (Isotropic Multiple Scattering Approximation) which allow us to model the phase function at VIS-IR (visible-infrared) wavelengths as well as the spectra taking into account various types of mixtures of surface materials. Thanks to this method we have been able to constrain the size of water ice particles covering the surface, the amount of organic contaminants, the large scale surface roughness and the opposition effect surge. From our analysis it appears that wavelength dependent parameters, e.g. opposition surge width (h) and single-particle phase function parameters (b, ν), are strongly correlated to the estimated single-scattering albedo of particles. For Rhea the best fit solution is obtained by assuming: 1) an intraparticle mixture of crystalline water ice and a small amount (0.4%) of Triton tholin; 2) a monodisperse grain size distribution having a particle diameter $a_m = 38 \mu\text{m}$; and 3) a surface roughness parameter value of 33° . The study of phase function shows that both Shadow Hiding and Coherent Backscattering contribute to the opposition surge. This study represents the first attempt, in the case of Rhea, to join the spectral and the photometric analysis. The surface model we derived gives a good quantitative description of both spectrum and phase curve of the satellite. The same approach and model, with appropriate modifications, shall be applied to VIMS data of the other icy satellites of Saturn, in order to reveal similarities and differences in the surface characteristics to understand how these bodies interact with their environment.

1. Introduction and Rationale

The Cassini spacecraft completed its initial four-year mission to explore the saturnian system in June 2008. Since then it entered in the extended mission phase (*Cassini-Huygens Equinox Mission*), which will last until September 2010. During all these years the VIMS (Visual and Infrared Mapping Spectrometer) instrument on board Cassini extensively observed the saturnian moons. The VIMS experiment consists of two imaging spectrometers observing the same field of view in two spectral ranges (Brown et al., 2004; McCord et al., 2004): VIMS-V spectrometer covering the 0.35 - 1.05 μm range in 96 spectral channels with a spectral sampling of $\Delta\lambda = 7.3 \text{ nm/band}$ and spatial

resolutions of 500×500 (nominal) or 166×166 (high resolution) $\mu\text{rad} \times \mu\text{rad}$ /pixel; VIMS-IR channel covering the $0.885 - 5.1 \mu\text{m}$ range with 256 bands, a spectral sampling of $\Delta\lambda \approx 16 \text{ nm/band}$ and spatial resolutions of 500×500 (nominal) or 250×500 (high resolution) $\mu\text{rad} \times \mu\text{rad}$ /pixel (Miller et al., 1996).

VIMS collected both resolved and disk-integrated spectra of the moons in a wide range of observing conditions (solar phase angle and hemispheric coverage). While high spatial resolution observations of the satellites are essential to obtain compositional maps of the objects, the disk integrated observations are very useful to study the global properties of the surfaces and to point out correlations as well as differences among the various satellites.

The full disk observations constitute of a huge database with more than 1400 observations, obtained over a wide range of phase angles, for a total of 126000 spectra, covering the full VIMS spectral range. For a detailed description of the database see Filacchione et al. (2007, 2010) (in the following referred to as F2007 and F2010 respectively).

Spectrophotometry is a very powerful diagnostic tool in remote sensing to study the composition and the physical properties of the surfaces of objects under investigation. The amount of solar radiation, as a function of the wavelength, scattered from a surface towards the observer under varying observing conditions (incidence, emergence and phase angles) is a nonlinear function of several parameters such as the composition of the materials making up the surface, their grain size, the porosity and surface roughness of the interacting surface layers.

To retrieve quantitative information on these fundamental parameters of the surfaces, we need a multiple scattering model which provide approximate solutions to the radiative transfer in a particulate medium. The Hapke IMSA model (Hapke, 1993, 2002, 2008; Hapke et al. 2009) is one of several models developed to study the scattering properties of packed media (Lumme and Bowell, 1981; Drossart 1993; Shkuratov et al., 1999). It is an analytic two stream approximate

solution to the radiative transfer equation and it has been applied successfully to perform photometric corrections of imaging data (Hudson and Ostro, 1999; Domingue et al., 2009), to investigate physical properties of regoliths (Mallama et al., 2002; Buratti et al., 2004) and to estimate surface compositions of planetary surfaces (Cruikshank et al., 2001; Cruikshank et al., 2005; Poulet et al., 2002).

In F2007 and F2010 the authors have adopted an empirical method of spectral analysis to reduce the dimensionality of the spectra by mapping high dimensional data into a lower dimension while preserving the main features of the original spectra. This led to the definition of a number of “Spectrophotometric Indicators” which are able to synthetically describe the spectrum. For instance spectral slopes in the visible range are a useful indicator of the degree of purity of water ice with respect to the presence of contaminants, thus two of the selected indicators are the slopes in the blue range of the spectrum (350-550nm) and in the NIR (near infrared) range (550-1000nm). In the IR range the most prominent features are the water ice absorption bands; consequently the authors have selected the depth of the 1.2, 1.5, 2.0 and 3.0 μ m water ice bands as additional indicators.

The systematic analysis performed in F2007/F2010 on the basis of these indicators indeed pointed out several compositional trends within the satellites system and raised several questions which have not yet received a satisfactory answer. For instance:

- the correlation among Phoebe, Iapetus and Hyperion. The origin of the material that causes the albedo dichotomy of Iapetus has been the subject of a long standing debate (Buratti and Hicks, 2003; Spencer and Denk, 2010; Tosi et al., 2010). However, Clark et al. (2008, 2011b), showed that the visible colors and UV absorber are consistent with a single source with varying abundance of the contaminants. Key to solution of the problem was the discovery of Rayleigh scattering from small particles (Clark et al., 2008). From the VIMS

data the spectral behaviour in the VIS-NIR range shows similarities between Iapetus and Hyperion; while the IR spectra point out a strong correlation between the features observed on Iapetus and Phoebe.

- The Band Depth at 1.5 μm versus Band Depth at 2.0 μm trend is the result of the combined effect of ice contamination, due to “darkening agents” as well as variable grain sizes, but the relative contribution of the two effects could not be ascertained. However, Clark et al. (2011a, 2011b) show that the 1.5 and 2.0 μm ice band depth ratio is affected by the amount of sub-micron sized ice grains in the regolith.
- The symmetry of the 2-micron ice bands is unusual, being asymmetric toward longer wavelengths in spectra of the icy saturnian satellites (Clark et al., 2008) and in other icy objects (see review by Clark et al., 2011a). Clark et al., (2010b) showed that this asymmetry could be due to the presence of sub-micron ice grains and modelled the spectra using Hapke theory modified to include the diffraction component from those particles.

From this point of view the analysis performed in F2007 and F2010 represent a valuable empirical study to describe the global properties of the surfaces of the moons, however quantitative estimates on the nature (composition and physical properties) of the regolith require a full radiative transfer model. We have then set ourselves to work to this task (Ciarniello et al., 2010a, 2010b), and this paper describes the results we have obtained applying a radiative transfer model to the complete data set of Rhea’s full disk observations.

Rhea, with a radius of 764 ± 1.1 km (Thomas et al., 2006), is the second largest moon of Saturn; it orbits in the E ring with mean semimajor axis of 527070 km (see <http://ssd.jpl.nasa.gov> and reference therein); its mass is $M = (2.306481 \pm 0.000059) \times 10^{21}$ kg, which corresponds to a density

of $1232.8 \pm 5.4 \text{ kgm}^{-3}$ (Iess et al., 2007) and geometric albedo of the satellite is 0.83 at $0.51 \mu\text{m}$ (Pitman et al., 2010).

We have selected Rhea as the starting point for this analysis as it has the largest coverage in solar phase angle and thus allows to thoroughly test the model. Our approach is based on a two steps analysis: first a spectral fit is performed to retrieve the abundances of contaminants and ice grain size, then these properties are used to compute single-scattering albedo at each wavelength, whose values are adopted in the Rhea's phase function fit for the whole VIMS spectral range.

In section 2 we have described the method applied to model the phase curves and the spectra. In section 3 the selected dataset is described as well as the reduction data procedure. In sections 4 and 5 spectral and phase function fits respectively are analyzed. Section 6 concerns the feedback of phase function fit to the spectrum fit. Conclusions and suggested future work are given in section 7.

2. Hapke model

Hapke's IMSA (Isotropic Multiple Scattering Approximation) model has been widely used to describe both solar phase curve and spectral properties of various objects in the solar system (Buratti 1985; Bowell et al. 1989; Domingue et al. 1995; Domingue and Verbiscer 1997). In this paper we refer to Hapke (1993) in order to describe the spectrophotometric properties of Rhea. For our analysis we have chosen full-disk images of the satellite and the formula we applied to describe the object full disk reflectance (FDR) as a function of the phase angle g is straightforward derived by Eq. 10.40, p.275 in Hapke (1993):

$$FDR(g) = \int_{A(i,v)} r(i, e, g) S(i, e, g) \mu d\Omega = \left\{ \frac{1}{8} \left[1 - \sin\left(\frac{g}{2}\right) \tan\left(\frac{g}{2}\right) \ln\left[\cot\left(\frac{g}{4}\right)\right] \right] \right\} \left[(1 + B(g)) p(g) - 1 \right] w + 4r_0(1 - r_0) \left\{ + \frac{4}{3} r_0^2 \left[\frac{\sin(g) + (\pi - g) \cos(g)}{2\pi} \right] \right\} K(g, \bar{\theta})$$

(1.)

where $r_0 = (1 - \gamma)/(1 + \gamma)$ and $\gamma = \sqrt{1 - w}$.

The effect of porosity, which has been introduced in Hapke (2008), is not considered here, similarly to Warell and Davidsson (2010), in order to reduce the number of free parameters in the following inversion process. An improvement of the IMSA model is given in Hapke (2002). It provides a more accurate analytic expression of the Ambartsumian-Chandrasekhar function $H(x)$ which appears in the definition of the bidirectional reflectance $r(i, e, g)$. However, we adopted a linear expression for $H(x)$ in the derivation of eq. 1 (eq. 8.56, p.212 in Hapke (1993)), since this expression could be easily integrated. Eq. 1 represents the sum of the reflectances $r(i, e, g)$ of each point on the surface $A(i, \nu)$, which is both viewed by the instrument and illuminated by the Sun, as a function of the incidence (i), emergence (e) and phase (g) angles. Each term is weighted by the cosine of the emergence angle $\mu = \cos(e)$ which correctly projects the emitting area on the plane orthogonal to the emission direction, and by the term $S(i, e, g)$ which describes the large scale surface roughness (craters, depressions and other reliefs). Two mechanisms contribute to the emission process: single scattering and multiple scattering. The first one depends on the single-particle phase function $p(g)$, which describes how the light interacting with a particle is scattered. Actually the single-particle phase function is an average on a small but statistically significant given volume of particles. We modeled it assuming a double lobed Henyey-Greenstein (Henyey and Greenstein, 1941; Domingue and Verbiscer, 1997) phase function (Eq. 2) which depends on two parameters b and ν : the first one describes the angular width of both forward and back scattering lobes, while the second one describes their relative amplitude.

$$p(g) = \frac{1 + \nu}{2} \frac{1 - b^2}{(1 - 2b \cos g + b^2)^{\frac{3}{2}}} + \frac{1 - \nu}{2} \frac{1 - b^2}{(1 + 2b \cos g + b^2)^{\frac{3}{2}}} \quad (2)$$

Another term which depends on single scattering is the one that accounts for the opposition effect (OE), $B(g)$. It describes the observed non-linear increase in reflectance towards small phase angles. In this work we use the mathematical formulation developed to treat shadow hiding opposition effect SHOE, which depends on the parameters B_0 and h , respectively the amplitude and the angular width of the effect. Rigorously, B_0 can assume values in the 0-1 range, however we allowed B_0 to be greater than 1 in order to take into account coherent backscattering (CB), which is another mechanism contributing to OE (Roush, 1994). We choose not to model explicitly the CBOE to reduce the number of free parameters. The term $K(g, \bar{\theta})$ in (Eq.1) is the full disk correction due to large scale surface roughness. Its value is always less than 1 and decreases with increasing roughness parameter $\bar{\theta}$, which is an average slope of the facets composing the surface.

Spectral information is included in the single-scattering albedo $w(\lambda)$. This parameter represents the fraction of light interacting with the particle (light can be absorbed, scattered or diffracted) that undergoes only scattering. Its value is in the range 0-1 and depends on the medium optical constants n and k (which are respectively the real and the imaginary part of the refractive index $m=n+ik$), and on the grain size. Similarly to the case of single-particle phase function, the value of the single-scattering albedo is an average over a small but statistically significant volume of particles, and it is calculated as the ratio of the scattering and extinction efficiencies Q_S and Q_E . In close-packed particulate media with spherical grains much larger than the wavelength (which is the assumption we made in our analysis) the IMSA model assumes that diffraction is negligible. In that case the extinction efficiency is 1 (the cross section of the particle is equal to the geometrical cross section) and single-scattering albedo is equal to the scattering efficiency Q_S , which can be directly calculated in the Hapke model once that optical constants of end-members, type of mixing and grain size are fixed.

We have investigated three types of mixing: areal, intimate and intraparticle. *Areal mixing* (Fig. 1a) is obtained averaging the reflectance of different patches of surface covered with different materials:

$$r_{tot} = \sum_i p_i r_i \quad (3)$$

where r_i is the reflectance of i 'th component and p_i is the fraction of total surface covered.

Intimate mixing (Fig. 1b) describes a medium in which particles of different composition are mixed together : this kind of mixing is obtained through a weighted average of single-scattering albedos of the different types of grains:

$$w_{tot} = \frac{\sum_i p_i \sigma_i w_i}{\sum_i p_i \sigma_i} \quad (4)$$

where σ_i is the geometrical cross section of the i 'th particle type and p_i is the volume percentage of each component.

Intraparticle mixing (Fig. 1c) describes media in which inclusions of contaminants are embedded in a matrix of different optical properties. This kind of mixing is obtained with the Maxwell-Garnett rule (Maxwell-Garnett, 1904; Mallet et al.2005; Grundy, 2009):

$$\varepsilon_{eff} = \varepsilon_1 + 3\varepsilon_1 p_2 \frac{(\varepsilon_2 - \varepsilon_1)}{[\varepsilon_2 + 2\varepsilon_1 - p_2(\varepsilon_2 - \varepsilon_1)]} \quad (5)$$

where ε_1 and ε_2 are the complex dielectric constants of the matrix and of the embedded material respectively, p_2 is the fraction of contaminant and ε_{eff} is the effective complex dielectric constant of the particle. The dielectric constant is related to optical constants by the following relation:

$$m = \sqrt{\varepsilon} = n + ik \quad (6)$$

Once the medium optical constants and particle diameter a_m are fixed it is possible, following Hapke's model, to compute single-scattering albedo w for a given type of particles. We do not report the single-scattering albedo derivation but refer to Hapke (1993) for further details and final equations.

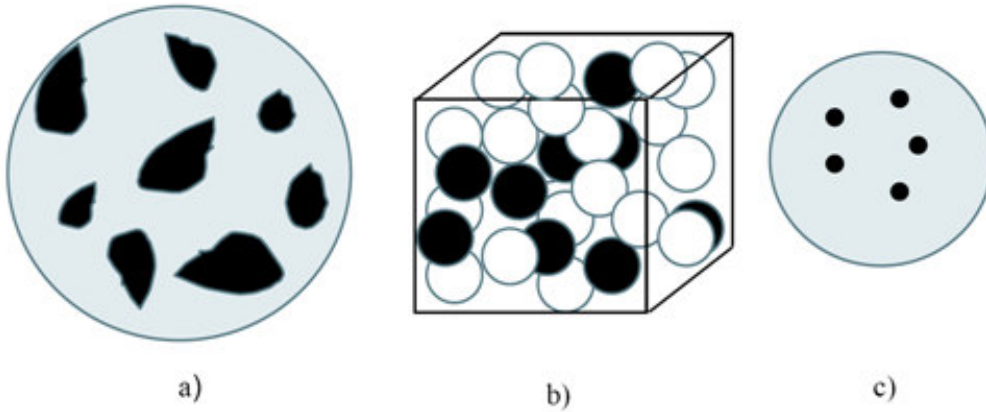


[FIGURE 1]

3. Observations and data reduction

Our dataset is composed of 140 observations acquired by VIMS in the period January 2005 - January 2008. Since Rhea exhibits a marked dichotomy between leading and trailing side (Verbiscer and Veverka, 1989; Buratti et al., 1998) we have selected only images in which the illuminated and observed area was more than 60% on the leading side, in order to study homogeneous regions of the satellite. With this limitation the total number of observations reduces to 111 with solar phase angles ranging from 0.08° to 109.8° .

VIMS collected full disk images of the satellite acquired at different spacecraft-target distance D both in normal and high-resolution modes. Accordingly, the satellite image size in the instrument

field of view can cover from a few tens to some hundreds of pixels. In order to produce phase function curves of the satellite at each wavelength we developed an IDL procedure that sums up the reflectances (I/F) of observed-illuminated pixels in the image, correcting them by the multiplicative factor $\delta\epsilon D^2 / R^2$ (where R is Rhea's radius and $\delta\epsilon$ is the solid angle subtended by the pixel). This factor represents the solid angle increment on the satellite surface times the emission angle cosine. The relation between observed data and FDR is:

$$\int_{A(i,v)} r(i, e, g) S(i, e, g) \mu d\Omega \approx \sum_j \left(\frac{I}{F} \right)_j \frac{\delta\epsilon D^2}{R^2} \quad (7)$$

where the subscript j identifies each single pixel.

In Fig. 2 Rhea full-disk normalized spectra acquired at various phase angle are plotted (for VIMS calibration uncertainties please refer to McCord et al. (2004)). All the spectra exhibit typical features of water ice (1.51, 2.2 and 3.1 μm absorption bands), however towards the UV region the shape of the spectrum strongly departs from the flat behavior of water ice producing a strong reddening. This feature has been traditionally assigned to the presence of organic contaminants as suggested by Cruikshank et al. (1998) and Poulet et al. (2002). However there is no clear additional signature in the IR, and this constrains the amount of contaminants to be at most few percent (Clark and Owensby, 1981). Clark et al., 2008 gave alternative explanations, including UV absorption by other compounds and very small grains (nano-phase) of opaque minerals such as hematite. Clark et al., (2011b) model the shape of the UV absorber with combinations of metallic iron (both large grained and nano-sized particles) and nano-phase hematite. A feature centered at 0.9 μm is present in all the spectra. This seems to be an artifact due to the data calibration process. However, the presence of this feature does not affect the global slope in VIS-IR region and doesn't introduce any offset between the two channels, and thus does not alter the results of the following analysis. The spectra show a certain dependence on observing geometry. The slope in VIS-NIR (around 1 μm) region and the band depth at 1.5 and 2.2 μm slowly increase with increasing phase angle, while this

trend is reversed at 3.5 μm . This peculiar behavior can be partially explained by varying the relative contributions of single and multiple scattering at different wavelengths (related to different values of the single-scattering albedo w as we will discuss later) and to a variation of single-particle phase function along the spectrum (even in this case related to w).

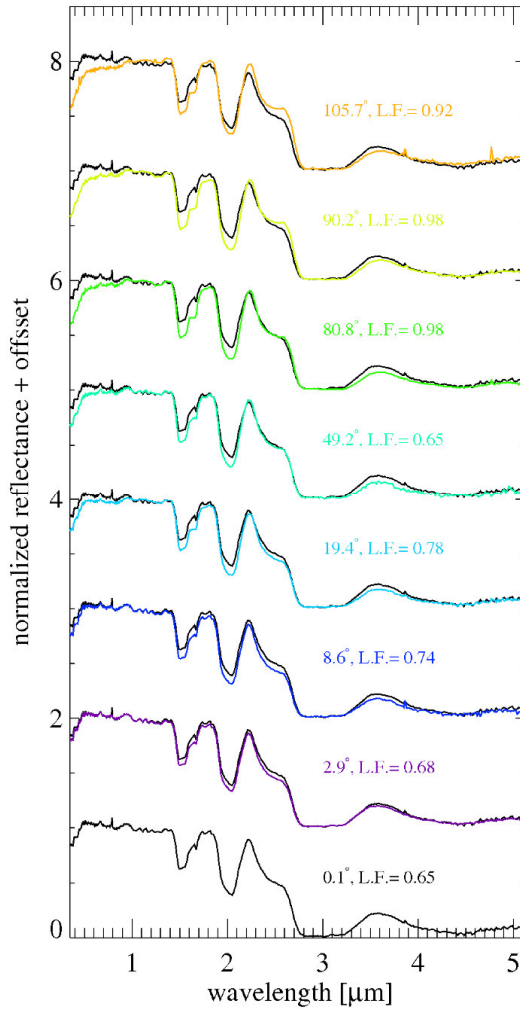


[FIGURE 2]

In Fig. 3 Rhea's normalized full-disk phase functions at various wavelengths are plotted. The coverage is fairly complete across the whole range, except for the 20°-40° region. The shape of the phase function is not constant with wavelength, which is obvious considering the dependence of the spectrum on phase angle mentioned above. In particular, the OE width and reflectance at

intermediate phase angles show a lot of variability while the differences decrease towards larger phase angles.

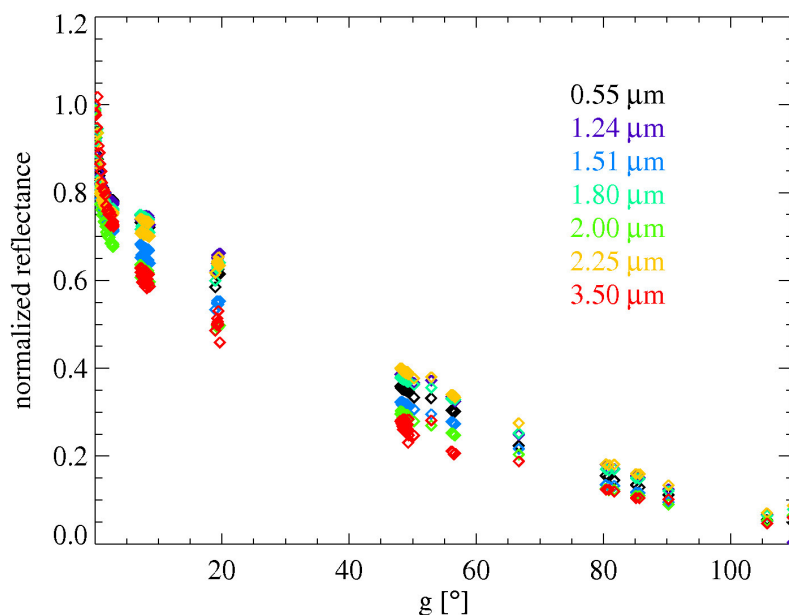


[FIGURE 3]

4. Spectral fit

The first step of our investigation is the interpretation of Rhea spectra in terms of physical characteristics of the surface involved in the scattering process. The principal properties that determine the observed spectral shapes are the composition (in this case water ice + contaminants) and the grain size. The presence of certain end-members is directly correlated with spectral signatures (absorption bands), while the grain size basically affects the depth of the bands as well as the IR slope (Clark and Lucey, 1984; Emery et al., 2005). In Hapke's model the spectral behavior is described by the single-scattering albedo w , whose value at each wavelength can be calculated once the end-members, their relative abundances, mixing mode and grain size distribution have been fixed. The single-scattering albedo cannot be directly compared to the observed spectra, because the

reflectance at each wavelength depends on single scattering, which relies on the single-particle phase function, and multiple scattering, which involves w in a non linear way, as shown in (Eq.1). Moreover, at low phase angle OE must be taken into account, while at high phase angles large scale surface roughness decrease the reflectance.

We have chosen to model Rhea's surface by means of a mixture of crystalline water ice and one organic contaminant. We used separately tholin from Khare et al. (1993), Triton tholin (McDonald et al., 1994; optical constants from Cruikshank, personal communication), Titan tholin (McDonald et al., 1994; Khare et al., 1984; optical constants from Cruikshank, personal communication) and hydrogenated amorphous carbon (ACH2) from Zubko et al. (1996). Optical constants for crystalline water ice are those derived by Warren (1984) (0.35-1.25 μm , 266.15 K), Mastrapa et al. (2008) (1.25-2.5 μm , 120 K), Mastrapa et al. (2009) (2.5-3.20 μm , 120 K) and Clark et al. (2011b) (3.20-5.12 μm , 120 K). We investigated areal mixing, intimate mixing and intraparticle mixing. In order to investigate spectral behavior of different mixtures without superimposing any grain size effect we studied only monodisperse particle diameter distribution (particles are all equal in size). This may lead to a non-unique solution, but as we shall see, provides information on the single particle phase function as a function of single particle albedo.

The other parameter fixed by the fitting procedure is the volume fraction of water ice p , with $p_c = 1-p$ being the amount of contaminants.

In order to retain a minimum number of parameters we decided to perform the spectral fit at high phase angle (90°) thus avoiding the OE surge. To remove the contribution of large scale surface roughness K we fitted normalized spectra (normalization was performed at 1 μm). This choice also allows to minimize the geometrical effects of single-particle phase function which at this stage is assumed isotropic, but may further reduce the uniqueness of the solution.

4.1 Optical constants

Summary plots of optical constants Vs wavelength used in this work are shown in Fig. 4-5. In the VIS-NIR range optical constants from Warren et al. (1984) pertain to ice at -7°C , whose temperature is too high if compared to Rhea's surface at 77 K (Pitman et al., 2010). However these values match reasonably well with the ones derived by Mastrapa et al. (2008) at 120 K. Optical constants in the $3.2\text{-}5.1\text{ }\mu\text{m}$ range are from Clark et al. (2011b) and have been computed starting from Mastrapa's values at the same wavelengths. The temperature difference between Rhea's surface and ice for which optical constants are determined introduces a tolerable error in our calculations, because it only minimally affects the results concerning grain size and contamination. The organic compounds, listed above, used to contaminate water ice, all have the effect of producing a red spectrum towards the UV (Fig. 5). Tholin from Khare et al. (1993) have been produced by plasma irradiation in an iced 6:1 mixture of H_2O and C_2H_6 at 77 K. Titan and Triton tholin are instead obtained in gaseous phase by irradiation of 0.9:0.1 and 0.999:0.001 $\text{N}_2\text{:CH}_4$ mixtures. ACH2 is obtained by arc discharge between carbon electrodes in H_2 atmosphere.

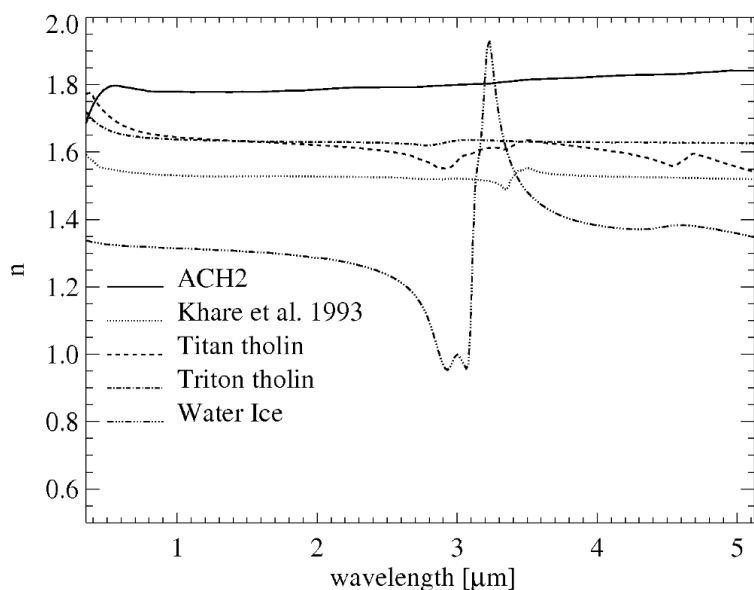


[FIGURE 4]

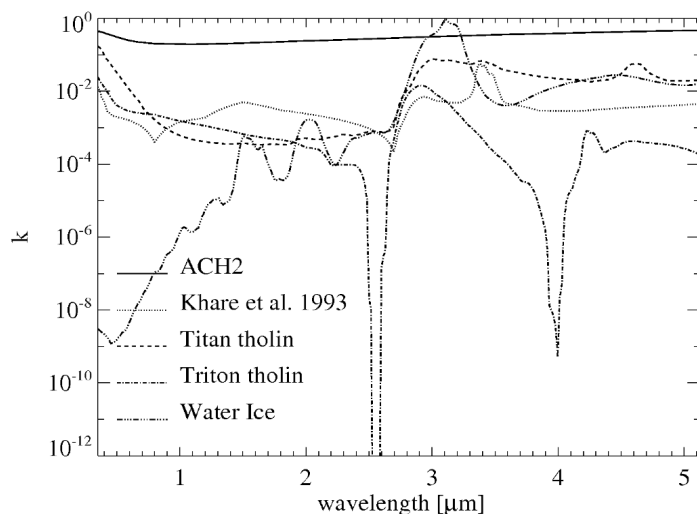


[FIGURE 5]

4.2 Areal mixing

We fitted observed spectra with different areal mixtures of two components where the main end-member is always water ice and the second is one among the selected organic contaminants. In areal mixing, the two different types of surface are characterized by different single-scattering albedo, and a beam of light interacts only with particles of the same composition. The resulting spectrum is a linearly-weighted average of the reflectances relative to the different regions. This kind of mixing is inefficient to produce the observed reddening towards UV. As an example we examine the cases of ACH2 and tholin (Khare et al., 1993). In the case of ACH2 the problem is mainly due to the fact that contaminant spectrum is not red enough to produce a sensible effect. It just reduces the reflectance across the whole spectrum without producing any absorption in the UV region, where water ice is strongly non-absorbing. In the normalized spectra this corresponds to an increment of reflectance of the darker wavelengths. This is shown in Fig. 6 (left panel) where the

results of five simulations with different abundances of ACH2 are plotted. The case of tholins (Fig. 6, right panel) is different because their spectra are not as flat as ACH2 far from UV region. In order to produce an effective feature towards short wavelengths many unobserved features are introduced in other regions of the spectrum. The outcome of this simulation is that the strong UV downturn observed in the Rhea spectrum it is not compatible with mixtures including compounds expected to be found on its surface. As an example, the best fit obtained with an areal mixture of water ice and Titan tholin is plotted in Fig. 7 (upper left panel). The results are similar using other types of contaminants. The fit, fairly good in IR, is completely lost in UV-VIS where a plateau is formed at the shortest wavelengths, missing the observed spectral downturn. Results for areal mixtures fits are summarized in Table 1.

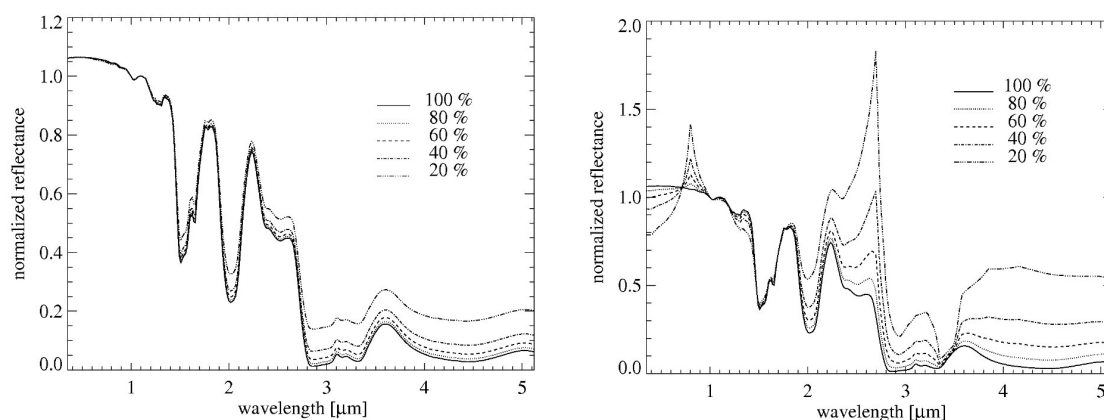
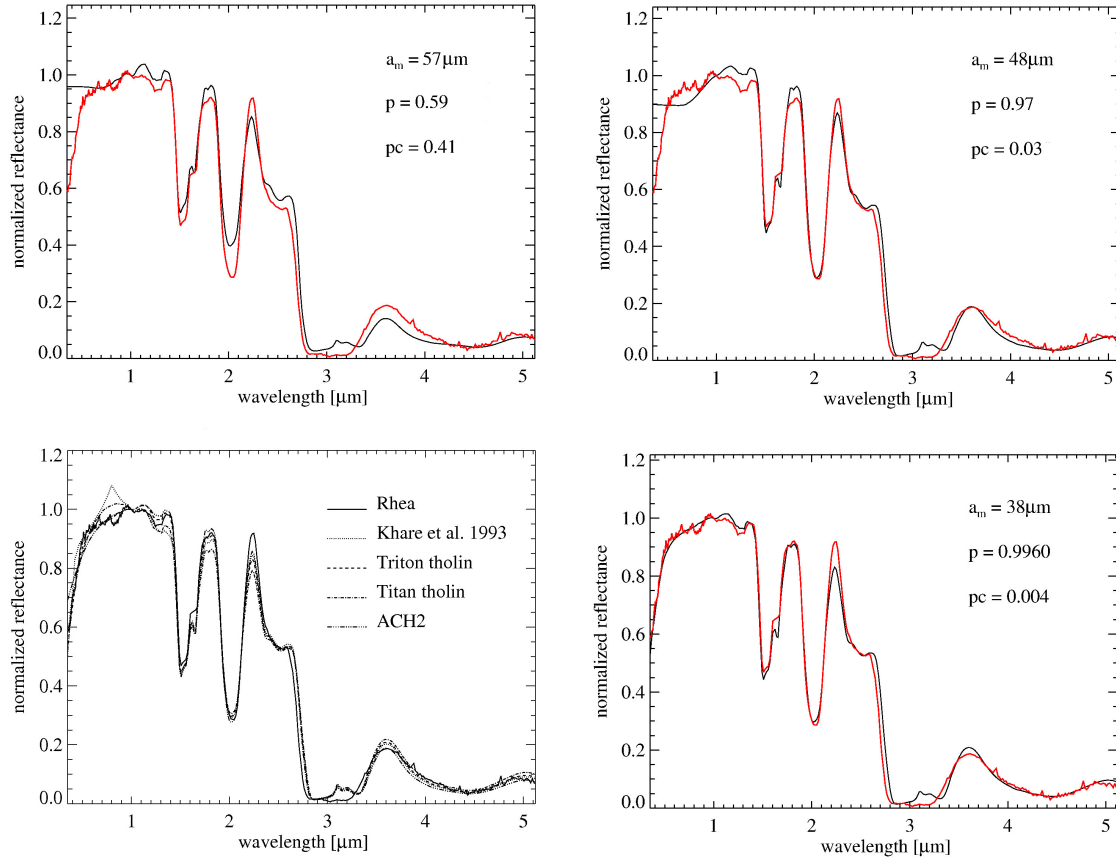


FIGURE 6]



[FIGURE 7]

[TABLE I]

4.3 Intimate mixing

Similar to the case of areal mixtures we obtained fits to Rhea's spectrum considering intimate mixtures of water ice and the available contaminants. In an intimate mixture, particles of different composition are in close contact (Clark, 1999), so this kind of mixing is also named "salt and pepper" (Poulet et al., 2003). A single ray of light entering the medium in a given position interacts both with water ice particles and contaminant particles. A small volume containing a statistically significant number of particles behaves as if it had an effective single-scattering albedo given by the

average of the albedo of the single particles. This kind of mixing is expected to be more efficient than areal mixing because at this stage spectral signatures (e.g. reddening) affect the effective single-scattering albedo and are stretched in higher order terms (w^2 , $w^3 \dots$) involved in the resulting reflectance, while in the case of areal mixtures, spectra of contaminants are only linearly combined. As a result, in intimate mixing, the darker component dominates the spectra signature (Clark, 1999). However, intimate mixing alone is still unable to reproduce the observed reddening of Rhea's spectrum for all the contaminants analyzed. Fig. 7 (upper right panel) shows the best fit obtained with an intimate mixture of water ice and Titan tholin. As with the result of the areal mixture the fit is acceptable in the IR but no reddening is produced towards the UV. The results of the fits are summarized in Table 2.

[TABLE II]

4.4 Intraparticle mixing

In this approach we consider the surface covered by identical particles of water ice with small inclusion of contaminants. The single particle behaves as if it had effective optical constants derived from a combination, given by the Maxwell-Garnett equation, of optical constants of ice and inclusions. For small amount of contaminants (which is the case of this work) the Maxwell-Garnett equation gives results similar to those obtained by a weighted average of the optical constants (Cuzzi and Estrada, 1998). This kind of mixing is the most efficient means of producing reddening because it exaggerates spectral differences, working directly with the complex refractive indices. As shown in Fig. 7 (bottom left panel), intraparticle mixing produces the required UV reddening with every contaminant considered in this work, although the type of reddening change from one contaminant to another. Extremely low concentrations of ACH2 (0.01%) are able to introduce UV

reddening, but the resulting spectrum falls too quickly towards short wavelengths before 1 μm and it is not steep enough below 0.4 μm . Titan tholin produces good fits at the shortest wavelengths but it is not sufficiently absorbing towards 1 μm . Tholin from Khare et al. (1993) shows a good agreement below 0.5 μm but has an unobserved feature at 0.8 μm . The best fit (Fig. 7, bottom right panel) is obtained with Triton tholin which reproduces even the change of slope in the spectrum around 0.5 μm . The particle size varies depending on the chosen contaminant. However, if we discard the results given by Titan tholin which produces the worst fit in the IR where the spectrum is more sensitive to grain size, we find that the particles diameter is limited to the range 40-50 μm . This diameter can be considered as an average size of particles, once we assume a monodisperse grain size distribution. Some discrepancies between the final fit and observed spectrum due to particle size are discussed in the next section where the best spectral fit is shown. Results for intraparticle mixtures fits are summarized in Table 3.

[TABLE III]

4.5 Best spectral fit

Considering the results presented in previous sections the best way to reproduce the spectral properties of Rhea is to assume an intraparticle mixture of 99.60 ± 0.05 % water ice and 0.40 ± 0.05 % Triton tholin, with a grain diameter of 38.0 ± 0.5 μm (Fig. 7, bottom right panel). Uncertainty on the derived values is related to the procedure we applied to perform the fit, as explained in Appendix A. Despite the small number of free parameters and end-members, the simulated spectrum fits well the observed spectrum. With such a low amount of tholin as a contaminant in the ice, other tholin absorption bands have a small effect on the infrared spectrum where ice is more absorbing. VIS reddening as well as water ice bands are very well reproduced. The secondary absorption band of crystalline water ice at 1.65 μm , which is shown in simulated spectrum, cannot be confirmed in VIMS data because in the wavelength range 1.60-1.66 μm the measured signal is affected by the presence of an order sorting filter on the detector. Consequently, the measured signal in that region

is replaced by an interpolated value. One of the stronger discrepancies is in the peak at $2.2\ \mu\text{m}$. This problem is shown in all the mixtures that have been analyzed so does not depend on the spectral properties of the contaminant but is instead most probably due to the chosen grain size distribution. In the case of monodisperse grain size distribution all the particles are equal and the contribution from smaller particles (with particle size similar or smaller than the wavelength), which certainly are present in a real distribution of sizes, is not considered. It must be noted that Hapke's model is developed in the geometric optics domain, so normally does not deal with grain size smaller than the wavelength. Clark et al. (2011b) have extended the Hapke model to include the diffractive scattering and absorption effects from sub-micron particles. Adopting a distribution of sizes which includes smaller particles it might be possible to reproduce the peak at $2.2\ \mu\text{m}$. Another part of the spectrum where the fit is lost for all the mixtures we deal with, is given by the absorption band at $3\ \mu\text{m}$. In simulated spectra the $3.1\ \mu\text{m}$ Fresnel peak is always visible, while in the measured spectra it completely disappears. The absence of the Fresnel peak cannot be completely attributed to the relative abundance of amorphous versus crystalline ice, as in amorphous ice the Fresnel peak doesn't fully disappear as shown by (Mastrapa et al., 2009). Moreover ground-based telescopic spectra of Rhea also attest to the crystalline nature of H_2O dominating its surface (Cruikshank et al. 2005; Emery et al. 2005). The absence of the Fresnel peak in Rhea's spectra (as in the case for the others icy bodies of the saturnian system) is probably due again to a grain size effect. In large particles light at $3\ \mu\text{m}$ is almost completely absorbed, given the high value of k and the longer path that light travels inside the grain. This implies that when we deal with big grains the light scattered by the particles is the one coming from surface reflections (that involves n) and which generates the Fresnel peak. Scattered light from smaller particles is the result of both surface reflection and internal reflection, thus the Fresnel peak is minimized. Since in our analysis the grain size is around $40\ \mu\text{m}$ and the contribution from small particles is neglected, the resulting spectrum exhibits an evident peak at $3.1\ \mu\text{m}$.

An intraparticle mixture of water ice and Triton tholin was adopted in Cruikshank et al. (2005) where a fit of Rhea spectrum was performed applying the Shkuratov model. It is interesting to note that both approaches require a comparable amount of embedded contaminant (0.4% in this work, 0.2% in Cruikshank et al. (2005)) and they both reproduces the reddening in the UV, even if the adopted spectral models and the surface modeling are different. It reinforces the idea that intraparticle mixing is the best approach to explain the UV feature and that Triton tholin is a reasonable candidate as the water ice contaminant.

5. Phase function fit

Results from the spectral fit allow us to determine the mixture (type of contaminant and mixing modality) and the grain size. The knowledge of these two parameters enables us to compute single-scattering albedo w which determines the spectral behavior of the observed surface. This quantity is involved in Eq. 1, which in our approach depends on 5 parameters (apart from w). The possibility to fix the single-scattering albedo reduces the complexity of phase function fit procedure and allows the decoupling of spectral effect from photometric ones.

A phase function fit at each wavelength available in VIMS range has been performed, using the surface model given by the best spectral fit that is represented by an intraparticle mixture of water ice and Triton tholin (99.6% - 0.04%), with 38 μm grain size. Parameters relative to the OE (B_0 , h) are allowed to vary along the spectrum because, as we mention in section 2, we want to take into account the CBOE as well which can depend on wavelength. Even the single-particle phase function (b, v) parameters can vary with wavelength because the single-scattering albedo has spectral variation and modifies the scattering properties of the grain. The large-scale surface roughness parameter ($\bar{\theta}$) is constant all over the spectrum because it accounts only for geometric effects due to surface structures. Details on the fit procedure are in Appendix. In Table 4 the best phase function fit variables for each VIMS channel are reported.

As we deal with particles that are in average larger than the wavelength, we do not expect a direct correlation between the values of parameters obtained by the fit and the wavelength itself. On the other hand, the single-scattering albedo, which determines the contribution of scattering in the light extinction process, plays a fundamental role for the photometric properties at a given wavelength.

This implies that the estimated parameters should be correlated with the single-scattering albedo rather than with the wavelength.

[TABLE IV]

5.1 Residuals

Fits are performed minimizing the residuals that are calculated for each wavelength following the formula:

$$res = \sum \left(\frac{r_i^m - r_i^c}{r_i^m} \right)^2, \quad (8)$$

where r_i^m is the measured absolute reflectance at i 'th phase angle while r_i^c is the value computed by the fit procedure (solar spectrum used to calibrate VIMS data is derived from Thekaekara (1973)). This kind of choice aims to give equal weight to the head and the tail of the full-disk phase function. Reconstructed full-disk phase functions for those wavelengths where the albedo is very low are often dominated by noise, and the corresponding fit parameters values are thought to have no physical meaning. Additionally, they produce high residuals because the model is unable to perform a satisfactory fit. For this reason we have considered for the following analysis only wavelengths with well determined full disk phase function and low value of the residuals. We found that for a residual value of 1 the full disk phase function can be considered well reproduced. From this point to the end of the paper we refer only to results relative to residuals lower than 1, unless explicitly written.

In Fig. 8 (upper left panel) fit residuals for each band are plotted against the value of single-scattering albedo computed for the correspondent wavelength. As we can see the accuracy of the fits increases with larger values of the single-scattering albedo. This effect is due to two reasons. The first is that for those wavelengths corresponding to a higher value of w the signal to noise ratio is typically higher and reconstructed phase functions are more accurate. The second is that at low values of the single-scattering albedo the dominating process is single scattering. In this regime the full-disk phase function is more sensitive to single-particle phase function and worse regression accuracy indicates that the Heyney-Greenstein expression is not able to completely describe the scattering process.

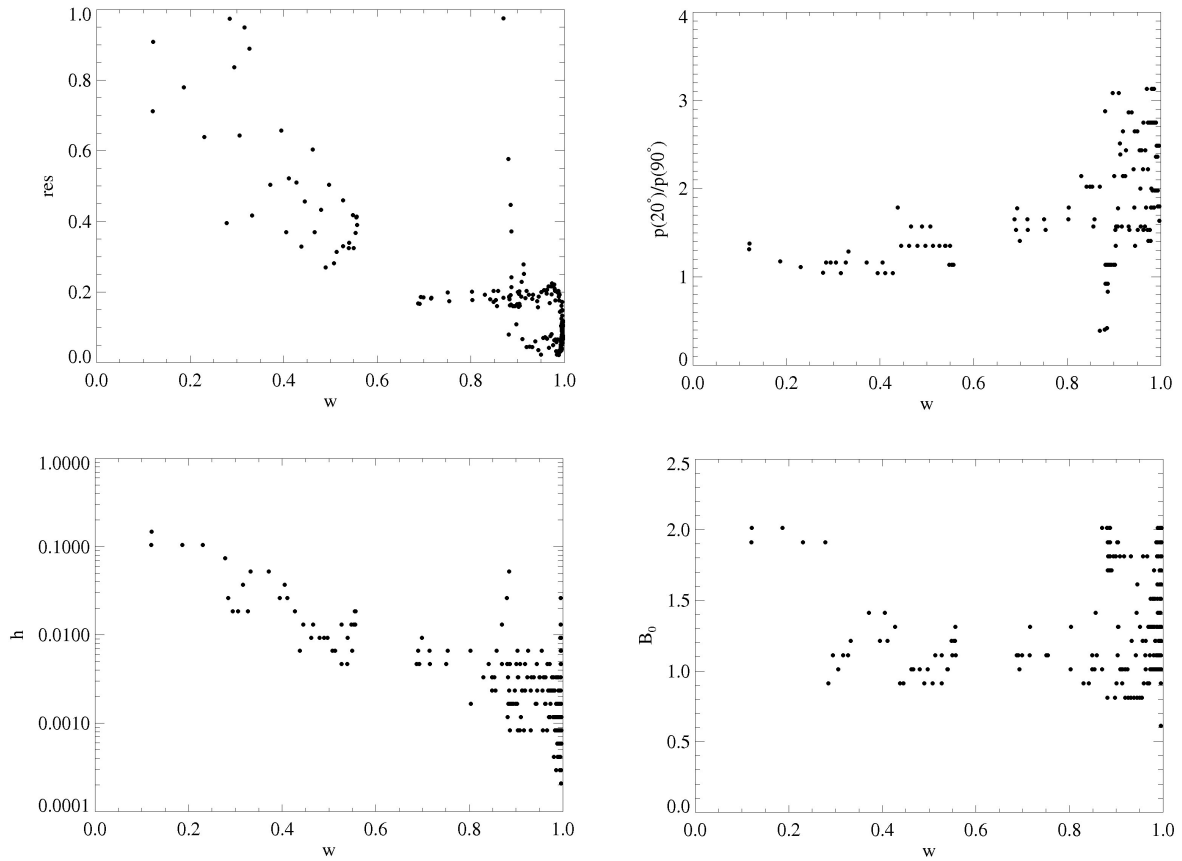
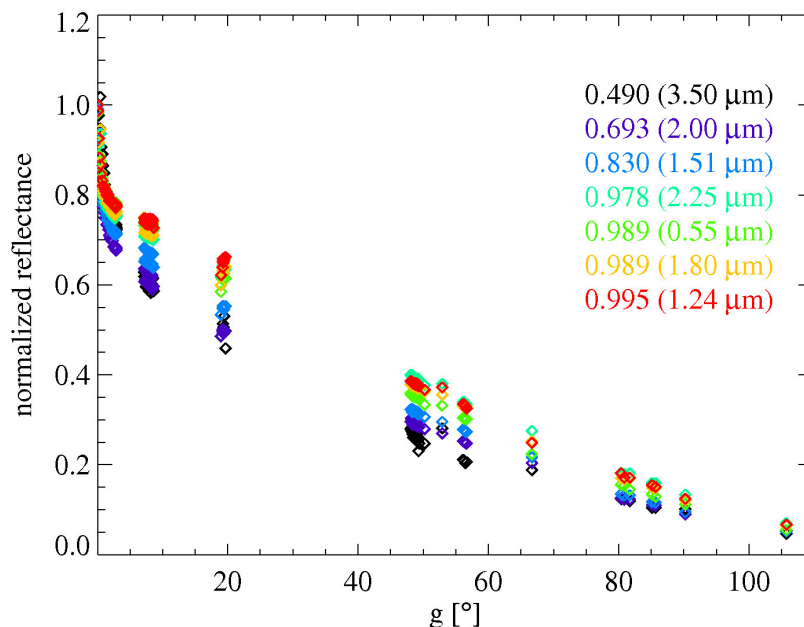


FIGURE 8]



[FIGURE 9]

5.2 Single-particle phase function

In fig.10 the distributions of b and v parameters are plotted. In these graphs it is shown how many times a certain value of the parameter occurs in a given range of w values. According to McGuire and Hapke (1995) a clear spherical particle should have $b \sim 0.5-0.7$ and $v \sim -0.9$. Most of our b values are slightly lower (0.3-0.4) as it's expected for real grains that are not perfectly spherical. Moreover b values should decrease with increasing absorption and it is what we found, since the fitted values shows a positive correlation with w . Concerning the v values, they are negative for a large part but greater than -0.9 (average value is -0.5), again as expected for not perfectly spherical particles.

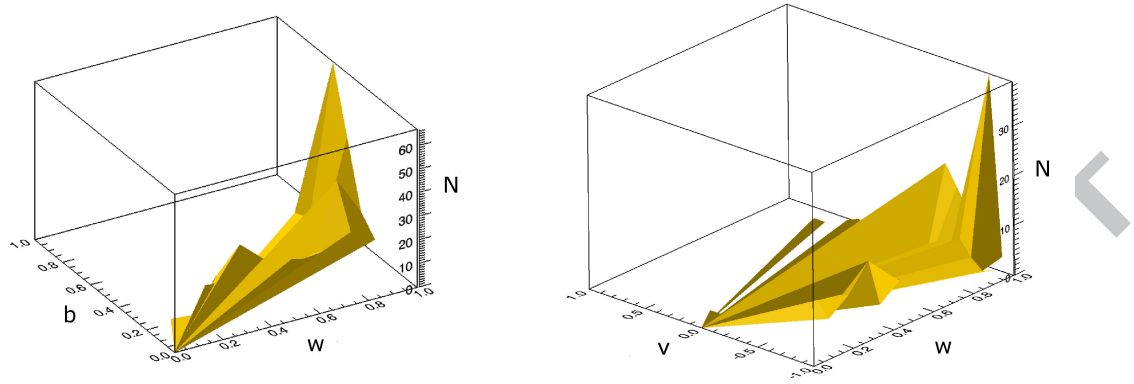


[FIGURE 10]

In order to show any relation between single-particle phase function and single-scattering albedo is useful to investigate the final shape of $p(g)$. In Fig. 8 (upper right panel), the ratio $p(20^\circ)/p(90^\circ)$ vs w is shown. This choice aims to point out the trend of the single-particle phase function at intermediate phase angles, avoiding the phase angle regions where the contribution of the OE and large scale roughness become relevant. The $p(20^\circ)/p(90^\circ)$ ratio increases with single-scattering albedo meaning that reflectance increases at intermediate phase angles (10° - 60°) for more transparent particles. This behavior can be explained by the possibility for a light ray to undergo multiple internal reflections in a non-absorbing particle, producing an higher backscattering lobe respect to a darker particle, where surface reflection dominates and produces a quite flat single-particle phase function at phases $< 90^\circ$ (Hapke, 1993, p. 77, Fig. 5.7a). This result is better shown in

Fig. 9, where normalized full disk phase functions are plotted ordered according to increasing values of single-scattering albedo (listed along with their relative wavelengths).

5.3 Opposition effect

As anticipated in previous sections we choose to model the opposition effect following the results developed in Hapke (1993) which consider only shadow hiding (SHOE). This model depends on two parameters (B_0 , h) which describes respectively the amplitude and angular width. Nonetheless, another mechanisms, coherent backscattering opposition effect (CBOE), has been recognized as contributing to the OE (Hapke et al., 1998; MacKintosh and Sajejev, 1998; Shkuratov et al. 1999b; Hapke, 2002). Given these reasons the interpretation of results concerning the OE is not trivial, because the two parameters (B_0 , h) must describe the contributes of both SHOE and CBOE. The two effects have different characteristics that help us discern between them. The major difference is that angular width of SHOE doesn't depend on wavelength, while the CBOE does (MacKintosh and Sajejev 1998; Hapke 2002). The second one is that the SHOE width extends up to 10° or more while the CBOE is limited to a width of 2° - 3° at most (Hapke et al. 1998, Shkuratov et al. 1999b). Additionally we must consider that SHOE is a single-scattering effect while the CBOE develops in a multiple-scattering process. Therefore, we expect that the SHOE dominates for wavelengths corresponding to low values of w while the CBOE dominates at wavelengths where w values is close to 1.

Figure 8 (bottom left panel) shows the plot h against w . The values of h spread over almost three orders of magnitude (0.0002-0.14) giving an OE half width $\Delta g \approx 2h$ ranging between 0.01° - 16° , and show a clear correlation with single-scattering albedo. At low values of w we have high h while the opposite is true when the albedo is low. This behavior reveals the presence of two competing

mechanisms in the OE: the CBOE for wavelengths with high value of albedo and the SHOE for the opposite case. This fact agrees with the argument that the CBOE depends on multiple scattering and the SHOE on single scattering. Moreover, we would expect that the h values at low w would be nearly constants, since SH is independent of wavelength. What we see, in fact, is that spreading reduces considerably towards small values of w with h approaching 0.1.

In the SH regime a rough estimation of the porosity of water ice particles on the surface can be computed from the following relation (Hapke 1993):

$$h \approx -\frac{3}{8} \ln(1-\phi) \quad (9)$$

where ϕ is the filling factor. The value of h we chose to use is 0.1, which is referred to low values of the single-scattering albedo, where single scattering dominate and the OE is due to SH. Moreover this value is almost constant with w , so it is independent of wavelength, which is what we expect for the SHOE. With this choice we obtain $\phi=0.23$. However, considering that a real grain size distribution has a non null dispersion and that the particle diameter we have measured is just an average value the filling factor can be higher. Assuming a grain size distribution of the form:

$$N(a) \propto a e^{-\frac{a}{a_m}} \quad (10)$$

we obtain $\Phi=0.35$. The derived porosity is then in the range 65-77 %. These values are lower than those derived in a similar study by Domingue et al. (1995). It must be noted that in Domingue's work the analysis was performed at 0.47 and 0.55 μm , where the single-scattering albedo is close to 1 and the CBOE contribution is important, reducing h and increasing the estimated porosity.

Regarding the amplitude of the opposition effect B_0 (Fig. 8, bottom right panel) we do not find any particular trend with w , apart from the fact that values have a larger spreading for single-scattering

albedo close to 1 tending to be higher respect to the rest of the spectrum. This could be an indication of the superimposition of the CB on SH, but a compensating effect due to the unsatisfactory modeling of the single-particle phase function (backscattering region) cannot be excluded.

5.4 Large-scale surface roughness

The large-scale surface roughness is characterized by the $\bar{\theta}$ parameter which Hapke (Hapke, 1993) interprets an average slope of the surface structures. This is the only parameter that doesn't depend on wavelength in our fit procedure. To constrain it we performed fits of full-disk phase functions for each value of $\bar{\theta}$ in the range 10° - 35° and chose the one that produced the smallest residual. We found a final value of $\bar{\theta}=33^{\circ}$ (we must point out that all the values above 30° gave similar fits). The result obtained seems too high if related to common slopes of craters and other topographic structures, and exceeds the values found by Domingue et al. (1995), while is close to the one found by Buratti (1985) for Mimas. Recent experimental analysis performed by Shepard and Helfenstein (2007), has shown that the value of $\bar{\theta}$ is not only affected by subpixel topography but also, and mainly, by roughness on the scale of particles clumping which can produce fairly high slopes, related to the angle of repose of the regolith, and consistent with our determination.

Typically, in phase function fit procedures, the estimated values of single-scattering albedo and surface roughness show a certain degree of correlation, which of course has no physical meaning and reveals a degeneration in the inversion process.

In our approach the evaluation of w comes from the spectral fit and it's completely independent on the determination of the roughness parameter, so the degree of degeneration of the regression is

reduced making the result more reliable. However, it must be noted, as pointed out in Davidsson et al. (2009), that the treatment of surface roughness in Hapke's theory relies on the assumption of "small mean slope" ($\bar{\theta} < 10^\circ$), which allows to obtain analytical solutions. The value we retrieved from the phase function analysis is far beyond this limit and must be considered with care.

Another issue is represented by the fact that in Hapke's theory multiple scattering between the facets composing the surface is neglected which is not applicable for high albedo materials and rough surfaces. In particular, icy surfaces have high albedo and, as shown in Shepard and Helfenstein (2007), the sub-centimeters scale roughness implies fairly large slope angles (typically above 10°).

This would limit the applicability of the roughness correction only to low albedo media, which is not the case of icy surface, unless the analysis is restricted to wavelengths where strong absorption bands are located (eg. 2.0 and 3.0 μm). In our analysis the derived $\bar{\theta}$ value produces good fits both for high and low reflectance values (e.g. 1 and 2 μm). This would imply that the effect of multiple scattering is less relevant than the "small mean slope" approximation.

6. Feedback on the spectral fit

The results of the phase function fits can be used to improve the spectral fit, which represented the starting point of our analysis. The spectral fit, as explained in section 4.0, was performed assuming an isotropic phase function and at phase angles large enough to avoid contributions from any OE. Now, for each phase angle it is possible to compute the absolute spectrum, removing the approximation of an isotropic single-particle phase function, including the OE and surface roughness. We have recalculated the spectrum at $g=90^\circ$, the one chosen to perform the starting spectral fit, and plotted it in Fig. 11. The agreement between the fitted spectrum and the measured one is almost perfect throughout the VIS-NIR region. Similar fits have been performed for each

spectrum (phase angle) of the dataset. As example the results relative to spectra at $g=2.1^\circ$ and $g=49.4^\circ$ are plotted in Fig. 12.

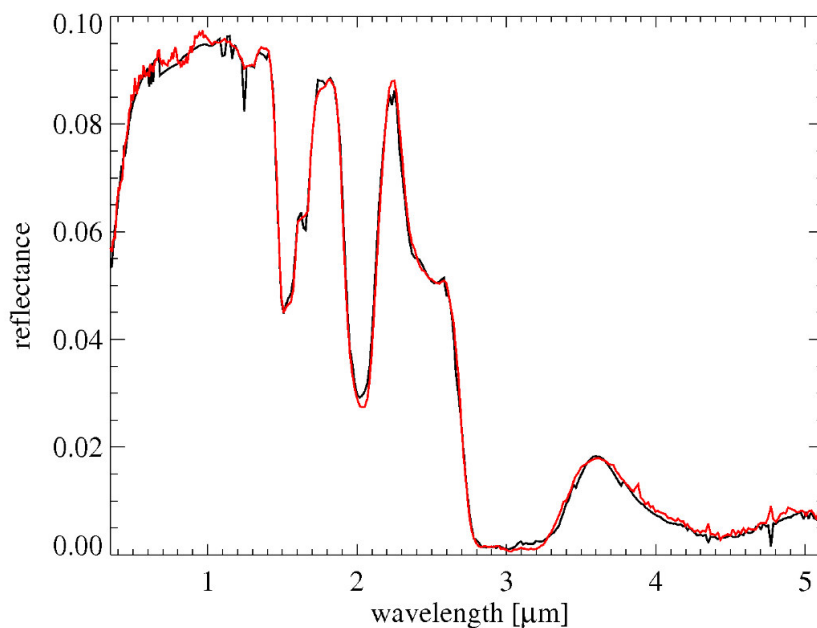


[FIGURE 11]

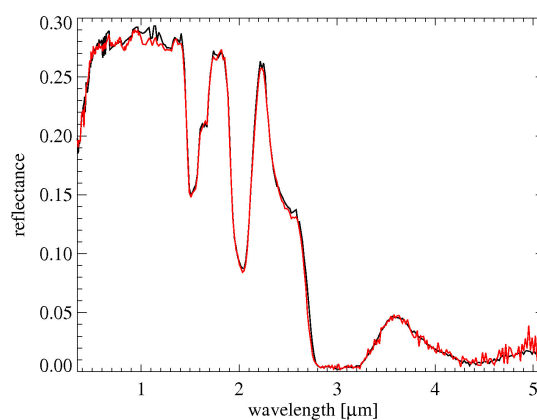
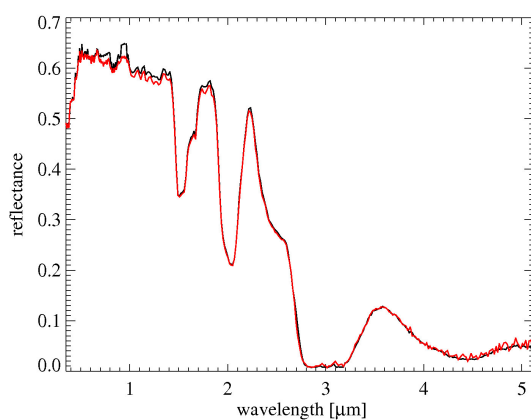


[FIGURE 12]

This high level of fit accuracy is possible because we deal with a large number of free parameters and this allows us to tune the reflectance at each wavelength. This represents also the limitation of this approach. In fact, any mismatches in the spectral fit due to grain size effects, as shown in section 4.5 for the reflectances at $2.2\mu\text{m}$ and $3.1\mu\text{m}$, or due to an incomplete knowledge of the ice optical constants, for instance, can be compensated by the contribution of the single-particle phase function. The spectral fit will be optimal but we shall be misled in the interpretation of the scattering mechanisms at work.

On the other hand, the trends observed in Fig. 8, 9 and 10 between phase curve parameters and the single-scattering albedo points out some degree of physical correlation among those variables. For instance, it is not totally unexpected to find that brighter surfaces have a narrower width of the opposition effect than darker surfaces; the contribution of multiple scattering within the grains attenuates the shadow hiding effect limiting it to a narrow region around the zero phase condition. Also, for planetary surfaces, the slope of the linear part is larger for brighter surfaces and this is consistent with the results shown in Fig. 8-9.

In other words, we could use these correlations to give preliminary estimates of the phase curve parameters to be used in the determination of the spectral fit; this approach can prove valuable also in case of incomplete or undersampled phase curves.

7. Summary and conclusions

We have studied surface spectrophotometric properties of Rhea, the largest icy satellite in the saturnian system. The analysis has been performed on spectra acquired by VIMS onboard Cassini, in the $0.35\text{--}5.12\mu\text{m}$ spectral range, covering the $0.08^\circ\text{--}110^\circ$ phase angle interval. This approach enabled us to investigate the compositional state of the ice covering the moon, the agglomeration state of the medium and the roughness properties. Hapke's spectral and photometric model has been

used for the analysis. Four different organic compounds have been investigated as water ice contaminants in order to model the reddening observed towards the UV. The best spectral fit in our model is represented by an intraparticle mixture of crystalline water ice (99.6 %) and Triton tholin (0.4%), with a grain size (diameter) of 38 μm . Major discrepancies between the measured and fitted spectrum can be addressed to a grain size effect, because our particle diameter distribution represents only the average size of the particles and therefore neglects the contribution of grains with dimensions comparable to or less than the wavelength.

Once the composition of the particles in the model was frozen it was possible to investigate the photometric properties of the satellite fitting the full-disk phase function at each wavelength. The picture that emerges is that the dominating parameter in the scattering process is the single-scattering albedo w , showing correlation with the single-particle phase function and OE. No particular dependence of OE on wavelength was found, as expected, considering that the typical grain size is larger than λ . The analysis of the OE indicates that both SH and CB are active, and their relative contribution depend on the single scattering albedo value. Measuring the OE angular width h in the SH regime we estimated a porosity varying between 65-77% .

The relatively high value of the roughness parameter ($\bar{\theta}=33^\circ$) is not compatible with the mean slope of surface structures like craters, depressions or other reliefs. This points to a correlation of $\bar{\theta}$ with roughness on smaller scale, possibly on the order of centimeters, confirming the Shepard and Helfenstein (2007) results, and providing an estimation of the regolith angle of repose.

The next step will be to apply the methodology described in this paper to the other full disk observations of the Saturn's icy satellites. From this point of view the huge VIMS dataset represents an extremely useful resource, given the large number of observations over a wide variety of geometric conditions. Our goal will be to determine the distribution of contaminants in the saturnian system and to point out compositional correlations among the moons. This analysis will represent a

useful tool for characterizing the effect of processes shaping the surfaces of these bodies: interactions with other moons, with the rings, and with the saturnian magnetosphere, as well as the surface activity of the moon itself.

As a future development we intend to investigate different kinds of grain size distributions involving even smaller particles (e.g. as done by Clark et al., 2011b). This new approach is beyond the limit of geometric optics applied in the present formulation of Hapke's model and requires to use Mie theory (Mie, 1908) to compute single-scattering albedo of the particles.

Acknowledgments

The authors M.C., F.C., G.F., P.C., A.C. and F.T. acknowledge support from an Italian Space Agency grant. The authors wish to thank the referees for their constructive comments.

APPENDIX: FIT PROCEDURE

Performing an inversion of a model with several free parameters is a challenging task. The most common problem is to discriminate between different solutions that give similar results. Fitting algorithms are able to find minima in the parameters space but it is difficult to discriminate between local and absolute ones. To overcome this problem we adopted a very simple and transparent method. We determined a grid in the parameter space through a quantization of the parameters over the full range of variability. For each point of the grid (a single combination of the parameters) we calculated the model prediction and compared it to the data. The best prediction represents the final

results of the fit. This method correctly finds the absolute minimum if the parameters space is sufficiently sampled. The quantization we chose is related to the degree of precision needed by the fit. At the same time the variability range for unbounded parameters has been fixed considering a range of values with physical sense.

Concerning the spectral fit we chose a quantization for the particle diameter a_m of 1 μm in a range extending from 10 to 100 μm ; we knew from previous analysis that higher values were unnecessary and that diameter values lower than 10 μm would have broken the limits given by geometric optics in Hapke model. The water ice mixing percentage range changes corresponding to the different mixtures, and in any case p was ≤ 1 . The quantization “step” of the parameters has been chosen as the minimum variation that could create an appreciable change in the output, consequently the fitted value can be assumed with an uncertainty of half “step”.

For the phase function fit the various parameters have been quantized in the following way:

$$B_0 \in [0;2], B_{0i} = i \cdot 0.1, i = 0,1,2,\dots,10$$

$$h \in [0.0001;0.1], h_i = 10^{(-4+0.15 \cdot i)}, i = 0,1,2,\dots,30$$

$$b \in [0;9], b_i = i \cdot 0.1, i=0,1,2,\dots,9$$

$$v \in [-1;1], v_i = -1 + i \cdot 0.1, i = 0,1,2,\dots,20$$

$$\bar{\theta} \in [10^\circ;35^\circ], \bar{\theta}_i = i, i=10^\circ,11^\circ,12^\circ,\dots,35^\circ$$

726 **Bibliography**

- 727 Bowell, E., Hapke, B., Domingue, D., Lumme, K., Peltoniemi, J., Harris, A.W., 1989. Application of
728 photometric models to asteroid. In: Binzel, R.P., Gehrels, T. and Matthews, M.S., (Eds.), *Asteroids II*,
729 University of Arizona Press, Tucson, pp. 524–556.
- 730 Brown, R.H., Baines, K.H., Bellucci, G., Bibring, J.-P., Buratti, B.J., Capaccioni, F., Cerroni, P., Clark, R.N.,
731 Coradini, A., Cruikshank, D.P., Drossart, P., Formisano, V., Jaumann, R., Langevin, Y., Matson, D.L.,
732 McCord, T.B., Mennella, V., Miller, E., Nelson, R.M., Nicholson, P.D., Sicardy, B., Sotin, C., 2004. The
733 Cassini Visual and Infrared Mapping Spectrometer (VIMS) investigation. *Space Sci. Rev.* 115 (1–4), 111–
734 168.
- 735 Buratti, B.J., 1985. Application of a radiative transfer model to bright icy satellites. *Icarus* 61, 208–217.
- 736 Buratti, B.J., Hicks, M.D., 2003. The Dark side of Iapetus: A model that finally works? *Bull. Am. Astron.*
737 *Soc.* 35, 915 (abstract).
- 738 Buratti, B.J., Mosher, J.A., Nicholson, P.D., McGhee, C.A., French, R.G., 1998. Near-infrared photometry of
739 the saturnian satellites during ring plane crossing. *Icarus* 136, 223–231.
- 740 Buratti, B.J., Hicks, M.D., Soderblom, L.A., Britt, D., Oberst, J., Hillier, J.K., 2004. Deep space photometry
741 of the nucleus of Comet 19P/Borrelly. *Icarus* 167, 16–29.
- 742 Ciarniello, M., Capaccioni, F., Filacchione, G., Coradini, A., Cerroni, P., Tosi, F., 2010a. VIS-IR spectral
743 modeling of Rhea and Enceladus. *EGU General Assembly 2010*, 6177 (abstract).
- 744 Ciarniello, M., Capaccioni, F., Filacchione, G., Coradini, A., Cerroni, P., Tosi, F., Stephan, K., 2010b.
745 Spectrophotometric analysis of Rhea surface scattering properties. *Lunar Planet. Sci. XLI*, 1643 (abstract).
- 746 Clark, R.N., Lucey, P.G., 1984. Spectral properties of ice-particulate mixtures and implications for remote
747 sensing. I – Intimate mixtures. *J. Geophys. Res.* 89, 6341–6348.
- 748 Clark, R.N., Owensby, P.D., 1981. The infrared spectrum of Rhea. *Icarus* 46, 354–360.
- 749 Clark, R.N., 1999, Chapter 1: Spectroscopy of Rocks and Minerals and Principles of Spectroscopy, *Manual*
750 *of Remote Sensing*, (A.N. Rencz, ed.) John Wiley and Sons, New York, p 3–58, 1999.
751 <http://speclab.cr.usgs.gov/PAPERS.refl-mrs/refl4.html>
- 752 Clark, R.N., Brown, R.H., Jaumann, R., Cruikshank, D.P., Buratti, B., Baines, K.H., Nelson, R.M.,
753 Nicholson, P.D., Moore, J.M., Curchin, J., Hoefen, T., and Stephan, K., 2008, Compositional mapping of
754 Saturn's satellite Dione with Cassini VIMS and implications of dark material in the Saturn system, *Icarus*,
755 193, 372–386.
- 756 Clark, R. N., R. Carlson, W. Grundy, and K. Noll, 2011a, Observed Ices in the Solar System. In: *Solar*
757 *System Ices*, Murthy Gudipati, ed., in press.
- 758 Clark, R. N., D. P. Cruikshank, R. Jaumann, R. H. Brown, J. M. Curchin, T. M. Hoefen, K. Stephan, C. M.
759 Dalle Ore, B. J. Buratti, G. Filacchione, K. H. Baines, P. D. Nicholson, 2011b, The composition of Iapetus:
760 Mapping Results from Cassini VIMS, *Icarus*, submitted.
- 761 Cruikshank, D.P., Roush, T.L., Bartholomew, M.J., Geballe, T.R., Pendleton, Y.J., White, S.M., Bell, J.F.,
762 Davies, J.K., Owen, T.C., de Bergh, C., Tholen, D.J., Bernstein, M.P., Brown, R.H., Tryka, K.A., Dalle Ore,
763 C.M., 1998. The composition of Centaur 5145 Pholus. *Icarus* 135, 389–407.

- 764 Cruikshank, D.P., Dalle Ore, C.M., Roush, T.L., Geballe, T.R., Owen, T.C., de Bergh, C., Cash, M.D.,
765 Hartmann, W.K., 2001. Constraints on the composition of Trojan Asteroid 624 Hektor. *Icarus* 153, 348-360.
- 766 Cruikshank, D.P., Owen, T.C., Dalle Ore, C., Geballe, T.R., Roush, T.L., de-Bergh, C., Sandford, S.A.,
767 Poulet, F., Benedix, G.K., Emery, J.P., 2005. A spectroscopic study of the surfaces of Saturn's large
768 satellites: H₂O ice, tholins, and minor constituents. *Icarus* 175, 268–283.
- 769 Cuzzi, J., R. Clark, G. Filacchione, R. French, R. Johnson, E. Marouf, L. Spilker, 2009. Ring particle
770 composition and size distribution, In: *Saturn after Cassini/Huygens*, Springer, DOI 10.1007/978-1-4020-
771 9215-2, pp. 459-509
- 772 Cuzzi, J.N., J. A. Burns, S. Charnoz, R. N. Clark, J. E. Colwell, L. Dones, L. W. Esposito, G. Filacchione, R.
773 G. French, M. M. Hedman, S. Kempf, E. A. Marouf, C. D. Murray, P. D. Nicholson, C. C. Porco, J. Schmidt,
774 M. R. Showalter, L. J. Spilker, J. N. Spitale, R. Srama, M. Sremcevic, M. S. Tiscareno, J. Weiss, 2010. An
775 evolving view of Saturn's dynamic rings. *Science*, 327, 1470 - 1475.
- 776 Davidsson, B.J.R., Gutiérrez, P.J., Rickman, H., 2009. Physical properties of morphological units on Comet
777 9P/Tempel 1 derived from near-IR Deep Impact spectra. *Icarus* 201, 335-337.
- 778 Domingue, D., Verbiscer, A., 1997. Re-analysis of the solar phase curves of the icy Galilean satellites. *Icarus*
779 128, 49-74.
- 780 Domingue, D.L., Lockwood, G. and Thompson, D., 1995. Surface textural properties of icy satellites: A
781 comparison between Europa and Rhea. *Icarus* 115, 228-249.
- 782 Domingue, D.L., Denevi, B.W., Ernst, C.M., Holsclaw, G.M., Izenber, N.R., McClintock, W.E., Murchie,
783 S.L., Robinson, M.S., 2009. Regional color photometry of Mercury's surface. *Lunar Planet. Sci. XL*, 1301
784 (abstract).
- 785 Drossart, P. 1993. Optics on a fractal surface and the photometry of the regoliths. *Planet. Space Sci.* 41, 381–
786 393.
- 787 Emery, J.P., Burr, D.M., Cruikshank, D.P., Brown, R.H., Dalton, J. B., 2005. Near-infrared (0.8-4.0 μm)
788 spectroscopy of Mimas, Enceladus, Tethys, and Rhea. *Astron. Astrophys.* 435, 353-362.
- 789 Filacchione, G., Capaccioni, F., McCord, T.B., Coradini, A., Cerroni, P., Bellucci, G., Tosi, F., D'Aversa E.,
790 Formisano, V., Brown, R.H., Baines, K.H., Bibring, J.P., Buratti, B.J., Clark, R.N., Combes, M., Cruikshank,
791 D.P., Drossart, P., Jaumann, R., Langevin, Y., Matson, D.L., Mennella, V., Nelson, R.M., Nicholson, P.D.,
792 Sicardy, B., Sotin, C., Hansen, G., Hibbitts, K., Showalter, M., Newman, S., 2007. Saturn's icy satellites
793 investigated by Cassini-VIMS. I. Full-disk properties: 350-5100 nm reflectance spectra and phase curves.
794 *Icarus* 186, 259-290.
- 795 Filacchione, G., Capaccioni, F., Clark, R.N., Cuzzi, J.N., Cruikshank, D.P., Coradini, A., Cerroni,
796 P., Nicholson, P.D., McCord, T.B., Brown, R.H., Buratti, B.J., Tosi, F., Nelson, R.M., Jaumann, R., Stephan
797 K., 2010. Saturn's icy satellites investigated by Cassini-VIMS. II. Results at the end of nominal mission.
798 *Icarus* 206 , 507-523.
- 799 Grundy, W.M., 2009. Is the missing ultra-red material colorless ice? *Icarus* 199, 560-563.
- 800 Hapke, B., 1993. *Theory of Reflectance and Emittance Spectroscopy*, Topics in remote sensing: 3,
801 Cambridge University Press, Cambridge, UK.

- 802 Hapke, B., 2002. Bidirectional reflectance spectroscopy. 5. The coherent backscatter opposition effect and
803 anisotropic scattering. *Icarus* 157, 523-534.
- 804 Hapke, B., 2008. Bidirectional reflectance spectroscopy. 6. Effects of porosity. *Icarus* 195, 918-926.
- 805 Hapke, B., Nelson, R., Smythe, W., 1998. The opposition effect of the moon: Coherent backscatter and
806 shadow hiding. *Icarus* 133, 89-97.
- 807 Hapke, B., Shepard, M.K, Nelson, R.M., Smythe, W.D., Piatek, J.,L., 2009. A quantitative test of the ability
808 of models based on the equation of radiative transfer to predict the bidirectional reflectance of a well-
809 characterized medium. *Icarus* 199, 210-218.
- 810 Hudson, R.S. and Ostro S.J., 1999. Physical model of Asteroid 1620 Geographos from radar and optical data.
811 *Icarus* 140, 369-378.
- 812 Iess, L., Rappaport, N.J., Tortora, P., Lunine, J., Armstrong, J.W., Asmar, S.W., Somenzi, L., Zingoni, F.,
813 2007. Gravity field and interior of Rhea from Cassini data analysis. *Icarus*, 190, 585-593.
- 814 Khare, B.N., Sagan, C., Arakawa, E.T., Suits, R., Callcot, T.A., Williams, M.W., 1984. Optical constants of
815 organic tholins produced in a simulated titanian atmosphere: From soft X-ray to microwave frequencies.
816 *Icarus* 60, 127-137.
- 817 Khare, B.N., Thompson, W.R., Cheng, L., Chyba, C., Sagan, C., Arakawa, E.T., Meisse, C., Tuminello, P.S.,
818 1993. Production and optical constraints of ice tholin from charged particle irradiation of (1:6) C₂H₆/H₂O at
819 77 K. *Icarus* 103, 290-300.
- 820 Lumme, K., and E. Bowell 1981. Radiative transfer in the surfaces of atmosphereless bodies. I. Theory.
821 *Astron. J.* 86, 1694-1704.
- 822 MacKintosh, F.C., Sajeev, J., 1988. Coherent backscattering of light in the presence of time-reversal-
823 noninvariant and parity-nonconserving media. *Phys. Rev. B* 37, 1884-1897.
- 824 Mallama, A., Wang, D., Howard, R.A., 2002. Photometry of Mercury from SOHO/LASCO and Earth. The
825 phase function from 2 to 170 deg.. *Icarus* 155, 253-264.
- 826 Mallet, P., Guérin, C.A., Sentenac, A., 2005. Maxwell-Garnett mixing rule in the presence of multiple
827 scattering: Derivation and accuracy. *Phys. Rev. B* 72, doi:10.1103/PhysRevB.72.014205
- 828 Mastrapa, R., Bernstein, M., Sandford, S., Roush, T., Cruikshank, D., Dalle Ore, C., 2008. Optical constants
829 of amorphous and crystalline H₂O-ice in the near infrared from 1.1 to 2.6 μm . *Icarus* 197 , 307-320.
- 830 Mastrapa, R.M., Sandford, S.A., Roush, T.L., Cruikshank, D.P., Dalle Ore, C.M., 2009. Optical
831 constants of amorphous and crystalline H₂O-ice: 2.5-22 μm (4000-455 cm^{-1}) optical
832 constants of H₂O-ice. *Astrophysical Journal* 701 , 1347-1356.
- 833
834 Maxwell-Garnett, J., 1904. Colours in metal glasses and in metallic films. *Philosophical Transactions of the*
835 *Royal Society of London. Series A* 203 , 385-420.
- 836 McCord, T.B., Coradini, A., Hibbitts, C.A., Capaccioni, F., Hansen, G.B., Filacchione, G., Clark, R.N.,
837 Cerroni, P., Brown, R.H., Baines, K.H., Bellucci, G., Bibring, J.-P., Buratti, B.J., Bussoletti, E., Combes, M.,
838 Cruikshank, D.P., Drossart, P., Formisano, V., Jaumann, R., Langevin, Y., Matson, D.L., Nelson, R.M.,
839 Nicholson, P.D., Sicardy, B., Sotin, C., 2004. Cassini VIMS observations of the Galilean satellites including
840 the VIMS calibration procedure. *Icarus* 172, 104-126.

- 841 McDonald, G.D., Thompson, W.R., Heinrich, M., Khare, B.N., Sagan, C., 1994. Chemical investigation of
842 Titan and Triton tholins. *Icarus* 108, 137–145.
- 843 McGuire, A., F. and Hapke, B. W., 1995. An experimental investigation of light scattering by large,
844 irregular particles. *Icarus* 113, 134-155.
- 845 Mie, G., 1908. Beiträge zur Optik trüber Medien, speziell kolloidaler Metallösungen. *Ann. Phys.* 330, 377
- 846 Miller, E., Klein, G., Juergens, D., Mehaffey, K., Oseas, J., Garcia, R., Giandomenico, A., Irigoyen, B.,
847 Hickok, R., Rosing, D., Sobel, H., Bruce, C., Flamini, E., DeVidi, R., Reininger, F., Dami, M., Soufflot, A.,
848 Langevin, Y., Huntzinger, G., 1996. The Visual and Infrared Mapping Spectrometer for Cassini. *Proc. SPIE*
849 2803, 206-220.
- 850 Pitman, K.M., Buratti, B.J., Mosher, J.A., 2010. Disk-integrated bolometric Bond albedos and rotational
851 light curves of saturnian satellites from Cassini Visual and Infrared Mapping Spectrometer
- 852 Poulet, F., Cuzzi, J.N., Cruickshank, D.P., Roush, T.L., Dalle Ore, C.M., 2002. Comparison between the
853 Shkuratov and Hapke scattering theories for solid planetary surfaces: Application to the surface composition
854 of two Centaurs. *Icarus* 160, 313-324.
- 855 Poulet, F., Cruickshank, D.P., Cuzzi, J.N., Roush, T.L., French, R.G., 2003. Compositions of
856 Saturn's rings A, B, and C from high resolution near-infrared spectroscopic observations
857 *Astron. Astrophys* 412, 305-316.
- 858 Roush, T.L., 1994. Charon: More than water ice? *Icarus* 108 , 243-254.
- 859
- 860 Shepard, M.K., Helfenstein, P., 2007. A test of the Hapke photometric model. *J. Geophys. Res.* 112, doi:
861 10.1029/2005JE002625.
- 862 Shkuratov, Y., Starukhina, L., Hoffmann, H., Arnold, G., 1999a. A model of spectral albedo of particulate
863 surfaces: Implications for optical properties of the Moon. *Icarus* 137, 245-246.
- 864 Shkuratov, Y., Kreslavsky, M.A., Ovcharenko, A.A., Stankevich, D.G., Zubko, E.S., Pieters, C., Arnold, G.,
865 1999b. Opposition effect from Clementine data and mechanisms of backscatter. *Icarus* 141, 132-155.
- 866 Spencer, J.R., Denk, T., 2010. Formation of Iapetus' extreme albedo dichotomy by exogenically triggered
867 thermal ice migration. *Science* 327, 432.
- 868 Thekaekara, M.P., 1973. Solar energy motion in space (SEMIS). In: *Proc. Symp. Solar Radiation Meas. and*
869 *Instrumentation*, pp. 414–442. SEE N76-15973 06-92.
- 870 Thomas, P.C., Helfenstein, P., Veverka, J., Burns, J., Porco, C., Denk, T., Turtle, E., 2006. Sizes, shape,
871 relaxation states and interior configurations of icy saturnian satellites. *Bull. Am. Astron. Soc.* 38, 621
872 (abstract).
- 873 Tosi, F., Turrini, D., Coradini, A., Filacchione, G., 2010. Probing the origin of the dark material on Iapetus.
874 *Mon. Not. R. Astron. Soc.* 403, 1113-1130.
- 875 Verbiscer, A., and Veverka, J. 1989. Albedo dichotomy of Rhea: Hapke analysis of Voyager photometry.
876 *Icarus* 82 , 336-353.

- 877 Warren, S.G., 1984. Optical constants of ice from the ultraviolet to the microwave. *Applied Optics* 23,1206-
878 1225.
- 879 Warrel, J. and Davidsson, B.J.R., 2010. A Hapke model implementation for compositional analysis of VNIR
880 spectra of Mercury. *Icarus* 209, 164-178.
- 881 Zubko, V.G., Mennella, V., Colangeli, L., Bussoletti, E., 1996. Optical constants of cosmic carbon analogue
882 grains – I. Simulation of clustering by a modified continuous distribution of ellipsoids. *Mon. Not. R. Astron.*
883 *Soc.* 282, 1321-1329.

884

885 **FIGURES CAPTIONS**

886 Figure 1. Schematic representations of two-components mixtures: areal (a), intimate (b) and
887 intraparticle (c). In a) the circle represents the field of view of the observing instrument, while in c)
888 the circle represents a single grain.

889

890 Figure 2. VIMS full-disk spectra of Rhea acquired at different phase angles, normalized at 1 μm .
891 An offset is added for clarity. The spectrum at each phase angle is compared to the spectrum at
892 0.08° (black curve). The leading fraction L.F. of each spectrum is reported.

893

894 Figure 3. Rhea's full-disk phase functions at various wavelengths. All the curves are normalized to
895 the value at minimum phase angle (0.08°).

896

897 Figure 4. Real part (n) of the refractive index for water ice and four organic contaminants:
898 hydrogenated amorphous carbon (ACH2), tholin from Khare et al. 1993, Titan tholin and Triton
899 tholin.

900

Figure 5. Imaginary part (k) of the refractive index for water ice and four organic contaminants: hydrogenated amorphous carbon (ACH2), tholin from Khare et al. 1993, Titan tholin and Triton tholin.

Figure 6. Simulated spectra of areal mixtures of water ice and ACH2 (left panel) and of water ice and Tholin from Khare et al. 1993 (right panel). The percentage of water ice is indicated. Spectra are normalized at 1 μm . Grain size is 50 μm .

Figure 7. *Upper left panel:* areal mixture best fit. It is obtained with water ice and Titan tholin. The percentages of water ice (p) and contaminant (pc) and the grain size are indicated. Observed spectrum is in red. Spectra are normalized at 1 μm . *Upper right panel:* intimate mixture best fit. It is obtained with water ice and Titan tholin. The percentages of water ice (p) and contaminant (pc) and the grain size are indicated. Observed spectrum is in red. Spectra are normalized at 1 μm . *Bottom left panel:* Summary plot of intraparticle mixtures fits. Rhea spectrum is the continuum line. All the mixtures are water ice + contaminant. Spectra are normalized at 1 μm . Grain sizes and compounds abundances are in Table 3. *Bottom right panel:* intraparticle mixture best fit. It is obtained with water ice and Triton tholin. The percentages of water ice (p) and contaminant (pc) and the grain size are indicated. Observed spectrum is in red. Spectra are normalized at 1 μm .

Figure 8. *Upper left panel:* phase function fit residuals at each wavelength against the single-scattering albedo. *Upper right panel:* single-particle phase function at 20° and 90° ratio for each wavelength against the single-scattering albedo. *Bottom left panel:* opposition effect width against

the single-scattering albedo. *Bottom right panel:* opposition effect amplitude against the single-scattering albedo.

Figure 9. Rhea full-disk phase functions at wavelengths relative to increasing value of the single-scattering albedo. Single-scattering albedo values and corresponding wavelengths are indicated. Curves are normalized at minimum phase angle (0.08°).

Figure 10. Distribution of fitted b (left panel) and v (right panel) values respect to the single scattering albedo. N represents how many times a certain value of the parameter is obtained in a given range of w values. The w range (0-1) is divided in intervals 0.1 wide.

Figure 11. Final absolute spectral fit at $g = 90.2^\circ$ ($p = 0.996$, $pc = 0.004$, $a_m = 38 \mu m$, intraparticle mixture). Isotropic single-particle phase function approximation has been removed and the correction due to roughness has been introduced. Observed spectrum is red.

Figure 12. *Left panel:* final absolute spectral fit at $g = 2.1^\circ$. *Right panel:* final absolute spectral fit at $g = 49.4^\circ$. The two simulations are obtained with an intraparticle mixture ($p = 0.996$, $pc = 0.004$, $a_m = 38 \mu m$). Isotropic single-particle phase function approximation has been removed and the correction due to roughness has been introduced. Observed spectrum is red.

945

946

947

948

Highlights

949

>Rhea's spectrum and phase function modeling. >Spectra from VIMS on board

950

Cassini spacecraft. >Intraparticle mixture of water ice and Triton tholin reproduces

951

observed reddening. >Determination of phase function parameters. >Dependence

952

of phase function parameters on single scattering albedo.

953

ACCEPTED MANUSCRIPT